



TECHNICAL ARTICLE

Oxidation Rate and Oxide Microstructures of Zr-1Nb-*x*Fe-0.05Cu-0.05Ge Alloys Corroded in 400 °C Superheated Steam

Yinjie Han, Jinlong Zhang, Dipeng Chen, Yang Hu, Meiyi Yao, and Bangxin Zhou

Submitted: 31 May 2022 / Revised: 26 August 2022 / Accepted: 25 September 2022 / Published online: 16 November 2022

The oxidation rate and the oxide film microstructures of Zr-1Nb-*x*Fe-0.05Cu-0.05Ge alloys ($x = 0.1, 0.15, 0.25, 0.35, \text{wt}\%$) corroded in superheated steam at 400 °C/10.3 MPa were investigated. Results show that the Zr-1Nb-0.35Fe-0.05Cu-0.05Ge alloy possesses the best corrosion resistance. As the content of Fe increases, the corrosion resistance of alloys is improved significantly and the main SPPs change from hcp-Zr(NbFe)₂SPPs to a mixture of hcp-Zr(NbFe)₂ and fcc-Zr(NbFe)₂ SPPs. Fe delays the development of the defects which lead to the formation of micro-cracks finally in oxide film. It also defers the evolution from columnar grains to equiaxed grains in the oxide film. [Zr-Nb-Fe]-type SPPs are initially oxidized into amorphous phases to reduce the grain boundary stress, which can delay the transformation of oxide film microstructure.

Keywords corrosion resistance, oxide microstructure, second phase particle, zirconium alloy

1. Introduction

Zirconium alloys are widely used as fuel cladding materials in water-cooled nuclear power reactors because of its low cross section for thermal neutron absorption, superior corrosion resistance and good mechanical strength. During its service, the corrosion resistance of fuel cladding material has been considered to be one of the most important properties for controlling the performance and safety of nuclear fuel rods (Ref 1-7). For this reason, researchers have developed Zr-2(Zr-1.5Nb-0.2Fe-0.1Cr-0.05Ni), Zr-4(Zr-1.5Sn-0.2Fe-0.1Cr), ZIRLO(Zr-1.0Sn-1.0Nb-0.1Fe), M5(Zr-1Nb-0.16O), E635(Zr-1.2Sn-1.0Nb-0.4Fe), HANA6(Zr-1.1Nb-0.05Cu) and NDA(Zr-1.0Sn-0.1Nb-0.28Fe-0.06Cr-0.01Ni) by adding different contents of alloying elements to improve the corrosion resistance of zirconium alloys in the past decades (Ref 7). The researchers found that the precipitation of the second phase in the zirconium alloy can affect its corrosion resistance. Liu et al. (Ref 8) studied the effect of Nb and Fe on the corrosion resistance. Their results show that the alloy with mostly [Zr-Nb-Fe]-type second phase particles (SPPs) has better corrosion resistance than the alloy with both [β-Nb]-type SPPs and [Zr-Nb-Fe]-type SPPs. The oxide film of zirconium alloys consists of columnar grains and equiaxed grains. Moreover, a higher

ratio of the columnar grains in the oxide film is associated with better corrosion resistance (Ref 9-14).

At present, there are many methods to improve the corrosion resistance of zirconium alloys. For example, ultrasonic impact shot peening is used to improve the corrosion resistance of Zr-Nb alloys (Ref 15-17). However optimizing the composition of alloys (i.e., alloying with other elements) is still a basic method to achieve high-performance zirconium alloys. Previous studies (Ref 18, 19) show that the corrosion resistance of Zr-1Nb alloy is enhanced significantly by alloying with low content of Ge or Cu in superheated steam at 400 °C/10.3 MPa. Fe changes the assessment of the solid solubility limit for Nb in α-Zr (Ref 20). The corrosion resistance of zirconium alloys is improved when Fe is at a range of more than 0.2wt% (Ref 21). Researchers found that Zr-1Nb-0.4Fe showed the optimal corrosion resistance in out-of-pile corrosion behavior among Zr-1Nb-*x*Fe alloys (Ref 22, 23). While β-Nb is the main SPPs in Zr-1Nb alloy, [Zr-Nb-Fe]-type is the main SPPs in Zr-1Nb-0.4Fe alloy. It is concluded that Fe is the main factor that influences the composition and structure of the precipitates in the Zr-1Nb-*x*Fe alloys. Unfortunately, the studies on the impact of Fe on the corrosion resistance of zirconium alloys are not systematic. Even worse, its influence mechanism is not clear.

This paper aims to understand the effect of Fe content on the corrosion resistance of Zr-1Nb-*x*Fe-0.05Cu-0.05Ge ($x = 0.1, 0.15, 0.25, 0.35, \text{wt}\%$) alloy. The oxidation rate and oxide microstructures of these alloys corroded in superheated steam at 400 °C/10.3 MPa are investigated.

2. Materials and Experiments

Different amounts of Fe with a certain amount of Zr, Nb, Cu and Ge were added to Zr-1Nb-0.15Fe alloy to prepare Zr-1Nb-*x*Fe-0.05Cu-0.05Ge ($x = 0.1, 0.15, 0.25, 0.35, \text{wt}\%$) alloys. The chemical composition of Zr-1Nb alloys containing Fe (Zr-1Nb-

Yinjie Han, Jinlong Zhang, Dipeng Chen, Yang Hu, Meiyi Yao, and Bangxin Zhou, Institute of Materials, Shanghai University, Shanghai 200072, People's Republic of China; and Laboratory for Microstructures, Shanghai University, Shanghai 200444, People's Republic of China. Contact e-mail: jlzhang@shu.edu.cn.

Table 1 Chemical compositions of Zr-1Nb-xFe-0.05Cu-0.05Ge alloys (wt%)

Alloy	Nb	Fe	Cu	Ge	Zr
Zr-1Nb-0.1Fe-0.05Cu-0.05Ge	0.94	0.09	0.069	0.056	Balance
Zr-1Nb-0.15Fe-0.05Cu-0.05Ge	1.03	0.13	0.064	0.055	Balance
Zr-1Nb-0.25Fe-0.05Cu-0.05Ge	1.12	0.27	0.065	0.052	Balance
Zr-1Nb-0.35Fe-0.05Cu-0.05Ge	1.04	0.38	0.055	0.066	Balance

xFe-0.05Cu-0.05Ge alloys) was analyzed by inductively coupled plasma atomic emission spectrometry (ICP-AES). The results were given in Table 1. Each experimental alloy ingot of 65 g was melted by the non-consumable vacuum arc melting method. To ensure the homogeneity of the composition, the ingots were overturned and remelted for 6 times. After being hot pressed at 700 °C, homogenizing annealing was conducted at 1030 °C for 40 min. Then the ingots were made into plates of about 1.4 mm in thickness through hot-rolling and β -quenched (1030 °C/40 min) to obtain fine SPPs. Then the final thickness of the plates was about 0.7 mm through cold-rolling. The final annealing step was conducted at 580 °C for 5 h to obtain a recrystallization. The specimens were chemically polished using a mixture of acid solution (30% H₂O, 30% H₂SO₄, 30% HNO₃ and 10% HF in volume fraction) before each annealing step. The corrosion tests were carried out in a static autoclave with superheated steam at 400 °C/10.3 MPa. The specimens were cleaned and pickled in the mixture of acid solution as mentioned above. Next, they were rinsed in cold tap water, then boiled in deionized water, and finally blow-dried with warm air. The specimen weight gain per unit surface area under a particular exposure time is defined as a mean value of 3–5 specimens.

The microstructures of the samples were observed by a JEM-2010F high-resolution transmission electron microscope (HRTEM). The chemical composition of SPPs was analyzed by an energy-dispersive-ray spectroscopy (EDS). The crystal structure and composition of the SPPs were identified by selected area electron diffraction (SAD) and the EDS analysis. The morphology of fracture surface and external surface of oxide films formed on the Zr-1Nb alloys containing Fe was characterized by a JEM-7500F high-resolution scanning electron microscope (HRSEM). The fracture surface samples of oxide films were prepared by breaking the oxide film on the edge of specimens after dissolving a part of the metal matrix in the interested area. A thin layer of Pt was sputtered on the oxide to improve the image quality of SEM observation.

The sample for the oxide microstructure observation on the cross section of the oxide film was prepared by a Helios-600i focused ion beam (FIB)(Ref 24, 25). High-angle annular dark field (HAADF) images were taken to determine the location of oxide/metal (O/M) interface and SPPs in the scanning transmission electron microscopy (STEM) model. The crystal structures of the oxide were identified by analyzing the lattice images from HRTEM micrographs by using Digital Micrograph software with the fast Fourier transform (FFT) patterns.

3. Experimental Results

3.1 Microstructures of the Zr-1Nb Alloys Containing Fe

Figure 1 shows the TEM images of the Zr-1Nb alloys containing Fe before corrosion. They are all partially recrystallized.

The SPPs with different sizes follow a banding distribution in the alloys, because the SPPs precipitate during the phase transformation from β -phase to α -phase after β -phase quenched. The banding distribution of SPPs is not destroyed during cold rolling because of low deformation rate. The EDS analysis results of typical SPPs (Fig. 1) in the alloys are presented in Table 2.

In order to determine the structure of the second phase in the alloy, selected electron diffraction (SAED) and energy-dispersive spectroscopy (EDS) analyses were performed on the second phase. In order to ensure the accuracy of the results, the same second phase is determined by diffraction patterns of two different rotation angles. Figure 2(c) and (f) shows f-Zr(Nb, Fe)₂ is mainly observed in the alloy containing 0.35Fe. Zr₂Cu and Zr₃Ge with tetragonal structure (t-Zr₂Cu and t-Zr₃Ge) are observed in the alloy containing 0.25Fe. As shown in Fig. 2(b) and (e), t-Zr₃Ge SPPs that are over 500 nm in size are also observed in the alloy containing 0.35Fe. Zr₃Ge can precipitate in the matrix of Zr-1Nb-xGe as the amount of Ge increases(Ref 26, 27). The solubility of Ge in α -Zr is less than 0.05wt%. Part of Ge will solubilize in [Zr-Nb-Fe]-type SPPs when the amount of Fe is less than 0.15wt%. Ge will precipitate as Zr-Ge SPPs, which is easy to grow up and form into Zr₃Ge SPPs with a large size when the amount of Fe increases. The increasing content of Fe may promote the precipitation of Cu and Ge solubilized in α -Zr. The results of corresponding SAD patterns of the SPPs are listed in Table 3. Results of EDS and SAD analysis show that there are three types of SPPs precipitated in the Zr-1Nb alloys containing Fe: [Zr-Nb]-type, [Zr-Nb-Fe]-type, and [Zr-M]-type (M = Cu, Ge, Fe). [Zr-Nb-Fe]-type precipitates are the main SPPs including [Zr-Nb-Fe] with face-centered cubic structure (f-Zr(Nb,Fe)₂) and [Zr-Nb-Fe] with hexagonal closed-packed structure (h-Zr(Nb,Fe)₂). h-Zr(Nb,Fe)₂ SPPs are observed in all the Zr-1Nb alloys containing Fe.

3.2 Weight Gains

Figure 3 shows the oxidation rate of the Zr-1Nb alloys containing Fe corroded in superheated steam at 400 °C/10.3 MPa for 400 d exposure. The weight gain of the alloy containing 0.1Fe is 260.1 mg/dm². Compared with the alloy containing 0.1Fe, the average weight gain decreases by 12.2% (0.15Fe), 19.8%(0.25Fe) and 22.5% (0.35Fe), respectively. The alloy containing 0.35Fe shows the optimal corrosion resistance among the alloys in this study. The content of Fe plays an important role in improving the corrosion resistance of these zirconium alloys.

3.3 External Surface Morphologies of Oxide Films

Figure 4 shows the SEM micrographs of the external surface morphology of the oxide film formed on the alloys corroded for 310 d exposure in superheated steam at 400 °C/10.3 MPa. Many micro-pores can be observed on the external

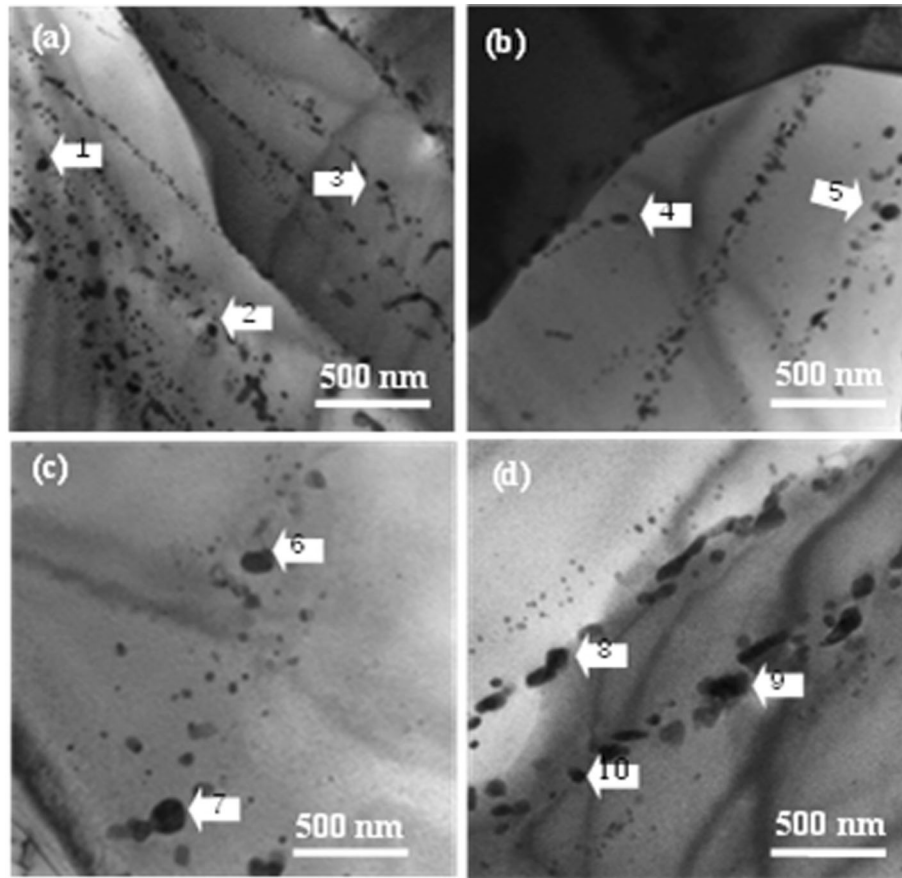


Fig. 1 TEM images of Zr-1Nb-xFe-0.05Cu-0.05Ge alloys (a) Zr-1Nb-0.1Fe-0.05Cu-0.05Ge, (b) Zr-1Nb-0.15Fe-0.05Cu-0.05Ge (c) Zr-1Nb-0.25Fe-0.05Cu-0.05Ge, (d) Zr-1Nb-0.35Fe-0.05Cu-0.05Ge

Table 2 EDS data statistical results of some typical SPPs in Fig. 1

Arrow	chemical component of SPPs, at.%						
	Zr	Nb	Fe	Cu	Ge	Cr	Nb/Fe
1	32.48	27.83	37.41	0.73
2	66.68	32.51	0.81	39.5
3	68.98	4.18	6.10	20.74	0.68
4	43.60	23.49	26.12	1.37	4.25	1.17	0.90
5	72.24	12.34	14.74	0.69	0.84
6	49.97	14.89	30.65	...	4.50	...	0.49
7	50.15	16.57	32.09	1.18	0.52
8	41.17	19.48	33.06	3.19	2.32	0.78	0.59
9	34.89	16.20	46.90	2.00	0.46
10	37.31	15.31	44.65	1.49	...	1.25	0.34

Note: Cr in Zr-1Nb-xFe-0.05Cu-0.05Ge alloys is from sponge zirconium.

surface of oxide film on the alloy containing 0.1Fe in Fig. 4(a). However, they do not show up on the external surface of the oxide film formed on the alloy containing 0.35Fe Fig. 4(b). The corrosion rate would be accelerated when O^{2-} ions diffuse into the O/M interface through these micro-pores(Ref 28). As a result, the protection of oxide film is lost gradually. The external surface morphology of the oxide film on the alloy containing 0.1Fe is fluctuated, while it is smooth for the alloy containing 0.35Fe. Micro-pores formed on the oxide film can be restrained by increasing the Fe content.

3.4 Fracture Surface Morphologies of Oxide Films

Figure 5 shows the fracture surface morphology of oxide films on the alloy containing 0.1Fe and 0.35Fe corroded for 130 d exposure. The thickness of oxide film on the alloy containing 0.1Fe is about 7 μm , while that value is about 4 μm for the alloy containing 0.35Fe. A series of micro-cracks parallel to the O/M interface are observed on the oxide fracture surface with quite obvious undulations in both alloys and it is more obvious in the alloy containing 0.1Fe in Fig. 5(a) and (b). The oxide

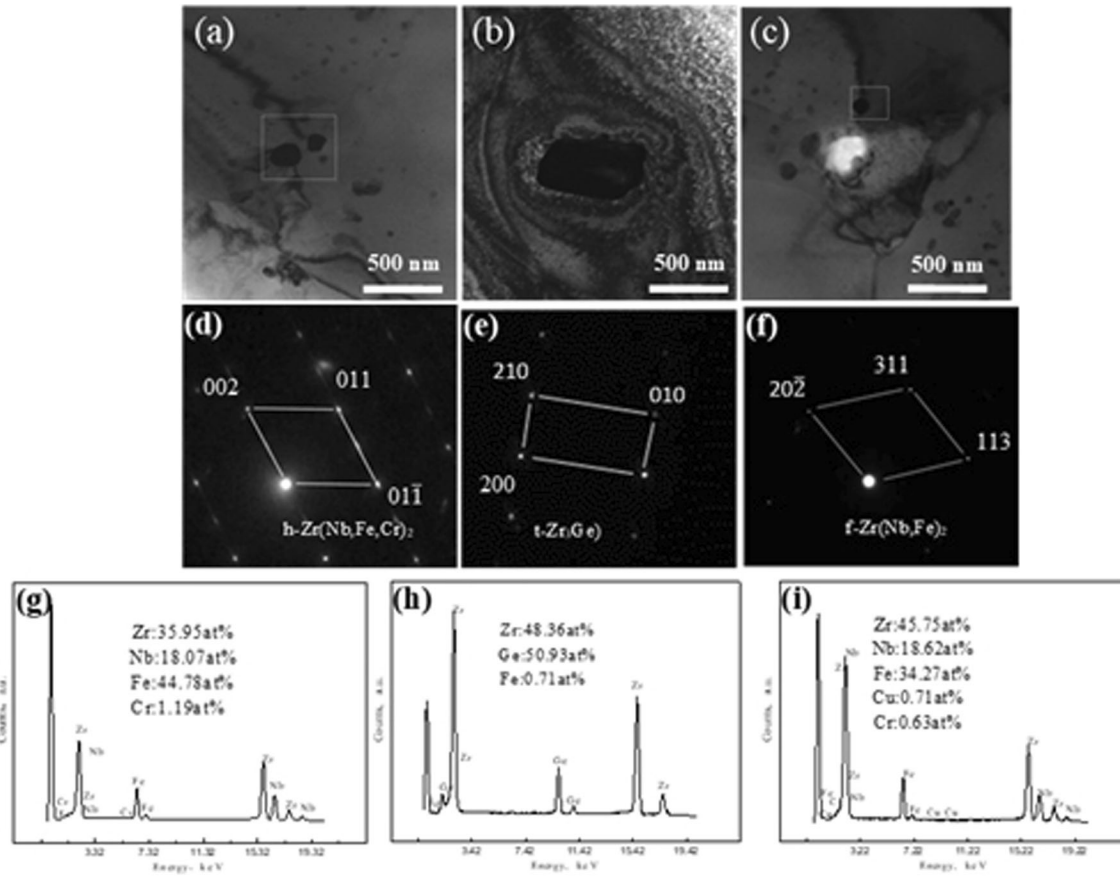


Fig. 2 TEM image of main SPPs (a) (b) (c), SAD pattern (d) (e) (f) and EDS data (g) (h) (i) in Zr-1Nb-xFe-0.05Cu-0.05Ge; (a) (d) (g) h-Zr(Nb,Fe)₂ SPPs in Zr-1Nb-0.25Fe-0.05Cu-0.05Ge alloy, (b) (e) (h) t-Zr₃Ge SPPs in Zr-1Nb-0.35Fe-0.05Cu-0.05Ge alloy, (c) (f) (i) f-Zr(Nb,Fe)₂ SPPs in Zr-1Nb-0.35Fe-0.05Cu-0.05Ge alloy

Table 3 Statistical result of SPPs in Zr-1Nb-xFe-0.05Cu-0.05Ge alloys

Alloys	SPPs					
	[Zr-Nb-Fe]					
	Freq	Size, nm	Struct	Nb/Fe	β-Nb	Others (minor)
x = 0.10	Major	30-200	hcp	~ 1.0	Minor	...
x = 0.15	Major	30 -200	hcp	~ 1.2	Minor	Zr ₂ Cu
x = 0.25	Major	30-200	hcp	~ 0.8	Minor	Zr ₂ Cu, Zr ₃ Ge
x = 0.35	Major	30 -200	hcp, fcc	~ 0.8	Minor	Zr ₃ Ge, Zr ₃ Fe

Note: Nb/Fe-atom ratio.

film of zirconium alloys is formed with a periodic change, which results in a layer structure(Ref 29). Micro-cracks are most likely to be formed between layers. The alloy containing 0.1Fe shows worse corrosion resistance because more micro-cracks between layers appear during corrosion transitions. Compared with the alloy containing 0.1Fe, the columnar grain of oxides on the alloy containing 0.35Fe is longer in the direction that is perpendicular to the O/M interface, more compact in structure, and more consistent in grain orientation. Furthermore, fewer grains are destroyed and transformed into equiaxed grains. The corrosion resistance of zirconium alloys is correlated to the characteristics of columnar grains (Ref 30). The growth of oxide film includes the process of the columnar

grain evolving into the equiaxed grain, in which the defects in columnar grains form new grain boundaries by diffusion and condensation(Ref 31, 32). It is indicated that Fe addition can stabilize the columnar grains to improve the corrosion resistance of zirconium alloys.

3.5 The Microstructure Observed from the Cross Section of Oxide Film

The cross-sectional sample of the oxide film on the alloy containing 0.35Fe for 42 d exposure was prepared by FIB. Figure 6a shows the HAADF image of the cross section of oxide films taken by HRTEM using the STEM mode. Figure 6b demonstrates the TEM image of the selected area in Fig. 6a.

HRTEM (EDS, in Table 4) images and the FFT image of three SPPs (named as P1, P2, and P3) were analyzed.

Figure 7a shows the HRTEM image and the FFT image of P1 SPP. It is concluded that the P1 SPP is $Zr(Nb,Fe)_2$ from the result of EDS analysis. Moire fringes are observed in some regions with a clear interface caused by stress concentration. The α -matrix is oxidized faster than SPPs and it would be restricted by the SPPs when the volume expansion of α -matrix takes place. Region A is identified as amorphous structure, whereas region B is identified as ZrO_2 with monoclinic structure (m- ZrO_2). Positions 1 and 2 in region C are identified as m- ZrO_2 and Fe_2O_3 with a cubic structure (c- Fe_2O_3), respectively. It is speculated that Fe diffuses to the outside during the oxidation of the SPPs.

Figure 7(b) shows the HRTEM image and FFT image of P2 SPP. It is observed that most part of the interface between SPP and ZrO_2 is indistinct, which indicates that the elements in this SPP have already diffused to the matrix that has been adequately oxidized. There are moire fringes beside P2 SPP. The FFT patterns of regions A and B show that they are amorphous structure, the mixture of amorphous structure, and crystal structure, respectively. Region C with an indistinct interface is identified as c- Fe_2O_3 . Region D and region E are

both identified as m- ZrO_2 . It is concluded that Fe is diffusing from inside of the SPP to its outside. At the same time, the SPP is initially oxidized into an amorphous structure, and then, oxidized into a crystal structure eventually.

Figure 7c shows the HRTEM image and the FFT image of P3 SPP, which is located beside a long crack. Its outlook is hard to diagnose. The SPP has been adequately oxidized, and its internal elements have diffused substantially. The FFT patterns of regions 1–5 inside the SPP show that regions 1,2,3 are identified as NbO_2 with tetragonal structure (t- NbO_2). In addition, the d values of crystal plane (031), (3 $\bar{1}$ 0), (321) in region 3 are 0.38 nm, 0.41 nm, 0.32 nm, respectively. A micro-pore is observed at the center of NbO_2 , which relieves the stress aroused by the oxidation from Nb to NbO_2 . The HRTEM image of region 4 is identified as Nb_2O_5 with monoclinic structure (m- Nb_2O_5), of which the d values of crystal plane (03 $\bar{1}$), (4 $\bar{2}$ 0), (41 $\bar{1}$) are 0.39 nm, 0.31 nm, 0.30 nm, respectively. The m- Nb_2O_5 of region 3 has a coherent relationship with the t- NbO_2 of region 4 in (03 $\bar{1}$)_m//(031)_{tet}, [126]_m//[$\bar{1}$ 39]_{tet}. It is concluded that t- NbO_2 is oxidized into m- Nb_2O_5 . m- ZrO_2 and the mixture of amorphous structure and crystal structure is observed around the SPP.

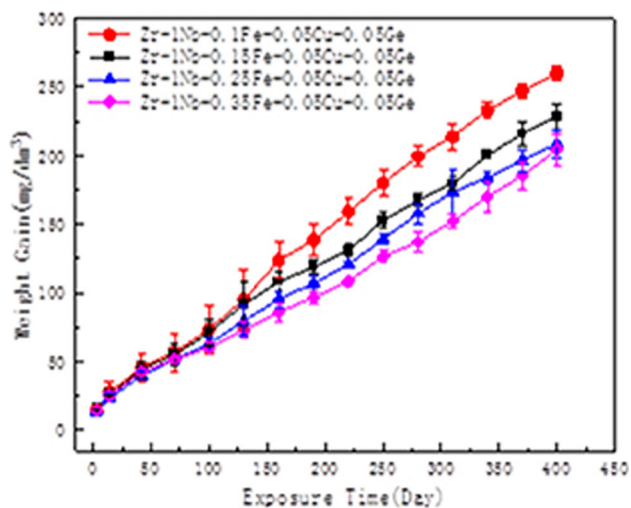


Fig. 3 Weight gain of Zr-1Nb-xFe-0.05Cu-0.05Ge alloys (red circle $x = 0.1$, black cubic $x = 0.15$, blue triangle $x = 0.25$, purple rhombus $x = 0.35$) corroded in superheated steam at 400 °C/10.3 MPa for 400 d exposure

4. Discussions

The corrosion resistance of the Zr-1Nb alloys containing Fe in superheated steam at 400 °C/10.3 MPa is improved as the Fe content is increased (Fig. 3). With the increase of Fe content, Fe can enhance the mechanical strength of oxide films, relieve stress by defects resulting from the oxidation of SPPs (Ref 33), and promote the stability of dense layer of oxide films (Ref 34). Because the P. B. ratio of Zr is 1.56, a large compressive stress will be generated in the oxide film due to the volume expansion in the process of Zr oxidation. Defects in the oxide film are produced under the compressive stress. Under the action of compressive stress and high temperature, defects diffuse, annihilate, and condensate. Also, vacancies are absorbed by the oxide grain boundaries to form micro-pores, which will develop into micro-cracks and decrease the protective characteristic of the oxide film (Ref 35). Therefore, the Fe addition could reduce the volume expansion of the oxide film, the compressive stress, and the pores as well as cracks in the oxide. In this study, it is observed that there are smaller ZrO_2 grains, fewer micro-pores and micro-cracks, and more consistent grain

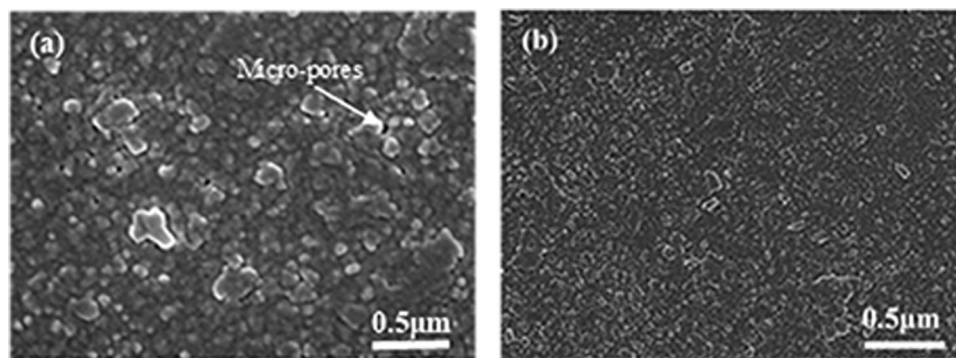


Fig. 4 External surface morphologies of the oxide films on Zr-1Nb-xFe-0.05Cu-0.05Ge alloys corroded in superheated steam at 400 °C/10.3 MPa for 310 d exposure (a) Zr-1Nb-0.1Fe-0.05Cu-0.05Ge, (b) Zr-1Nb-0.35Fe-0.05Cu-0.05Ge

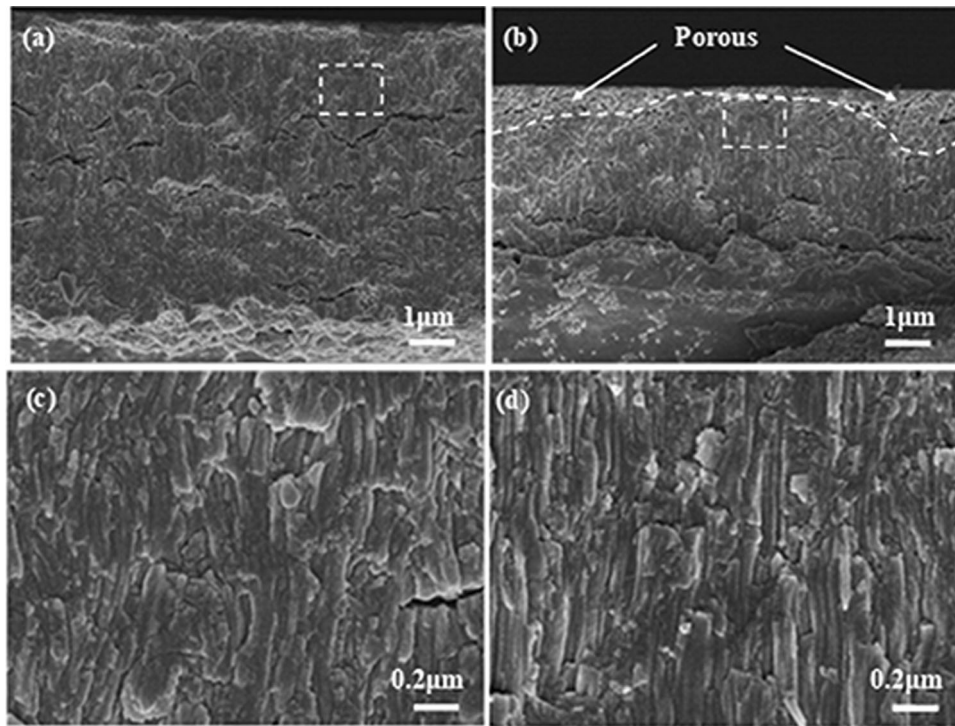


Fig. 5 The fracture surface morphologies of the oxide films on Zr-1Nb-0.1Fe-0.05Cu-0.05Ge (a) (c) and Zr-1Nb-0.35Fe-0.05Cu-0.05Ge (b) (d) alloys corroded in superheated steam at 400 °C/10.3 MPa for 130 d exposure

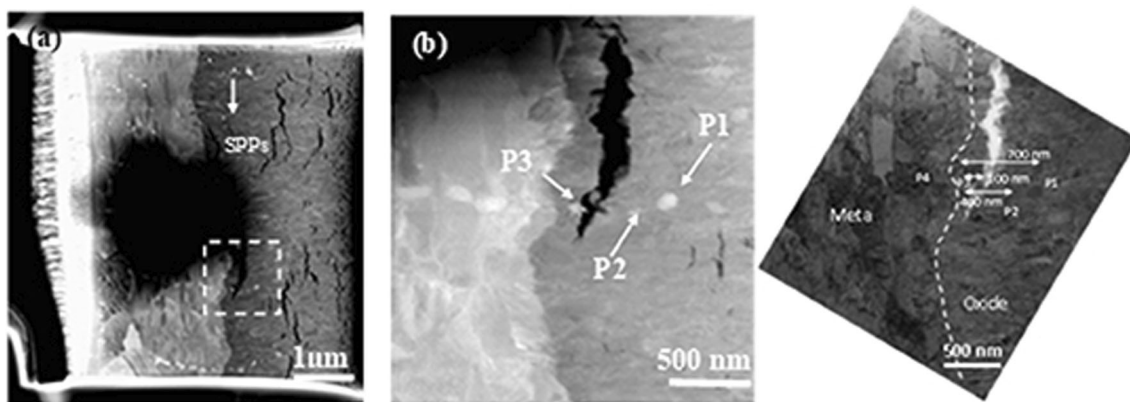


Fig. 6 Cross-sectional sample of oxide film of Zr-1Nb-0.35Fe-0.05Cu-0.05Ge alloy of 42 d exposure

Table 4 EDS data and SPPs size statistical result of P1 P2 and P3

NO	Zr	Nb	Fe	Ge	O	Nb/Fe	Distance
P1	49.67	31.98	12.70	1.16	4.49	2.5	700 nm
P2	69.86	19.74	6.90	0.92	2.59	2.9	400 nm
P3	75.61	14.65	6.06	...	3.68	2.4	100 nm

Note: atom ratio; Distance: distance to O/M interface

orientation in the oxide film formed on the alloy containing 0.35Fe than that formed on the alloy containing 0.1Fe (Fig. 4 and 5).

The type and size of the SPPs are important factors for affecting the growth and property of the oxide film. Part of Fe is

dissolved in α -Zr matrix, and the excessive Fe will precipitate as the SPPs because of its low solubility in α -Zr matrix. Fe will precipitate as [Zr-Nb-Fe] SPPs in zirconium alloys containing Nb. The structure of [Zr-Nb-Fe] SPPs transforms gradually from hcp to fcc as the Fe amount increases from 0.1 to 0.35 (Tab. 3). The ratio of Nb/Fe in SPPs drops as the Fe amount increases. As a result, the main structure of [Zr-Nb-Fe] precipitates transforms from hcp to fcc, which is in accordance with the observations of Kim et al. (Ref 36). Kim et al. found that [Zr-Nb-Fe]-type SPPs, precipitated as a face-centered cubic structure (fcc), were oxidized into a nanocrystalline structure, which can improve the corrosion resistance through stabilizing t-ZrO₂ and increasing the diffusion distance of O²⁻. Liu (Ref 8) found that the alloy with more [Zr-Nb-Fe]-type SPPs possessed better corrosion resistance in Zr-Sn-Nb-Fe alloys.

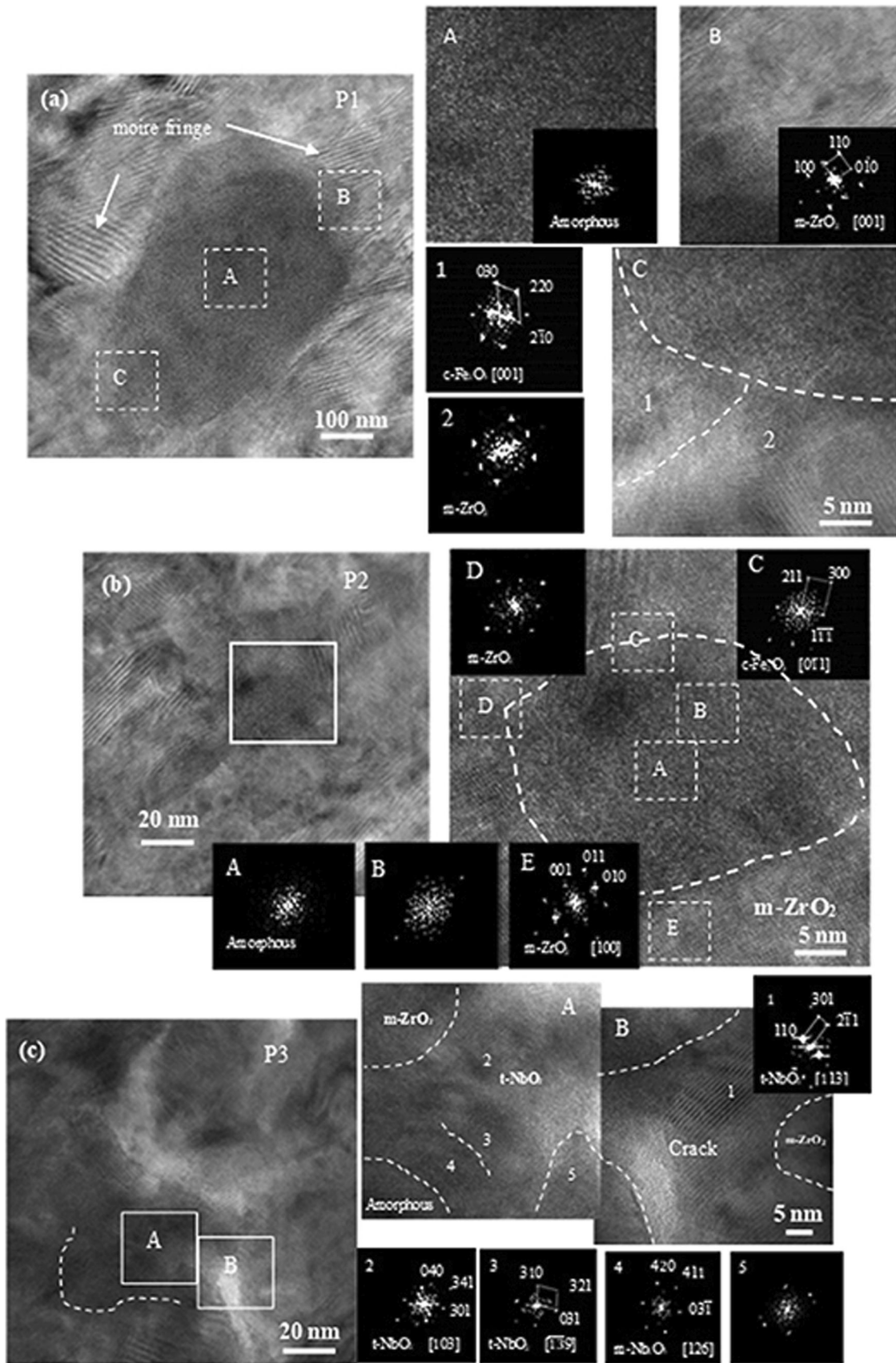


Fig. 7 Microstructure and FFT of the SPPs P1(a), P2(b) and P3(c) observed on the cross-sectional specimen of oxide film formed on Zr-1Nb-0.35Fe-0.05Cu-0.05Ge alloy at 400 °C/10.3 MPa for 42 d exposure.

[Zr-Nb-Fe]-type SPPs are partly oxidized into amorphous structure (Fig. 7). The compressive stress could be partially released by the formation of amorphous and t-ZrO₂ metastable phases (Ref 10), (Ref 31). Therefore, the formation of the amorphous phase can delay the transformation of microstructure of oxide film. At the same time, Fe is pushed out from the SPPs and then oxidized into Fe₂O₃. As the O²⁻ diffuses into the inner part of the SPPs, Nb is initially oxidized into NbO₂ and then further oxidized into Nb₂O₅. Amorphous phase could release the stress at the interface between SPPs and oxide film. Cao (Ref 37) proposed that continuous oxide film was formed on the surface of corrosion products. Less elements were ejected and volume expansion was lower after the oxidation of Zr. A compact and continuous oxide layer may form on the surface of matrix so that the diffusion rate of O²⁻ in ZrO₂ was reduced, which indicates an improved corrosion resistance.

The Pilling-Bedworth (P.B.) ratio represents the ratio of the volume of oxide to the volume of metal consumed. The P.B. ratio of Nb is 1.92 when Nb is oxidized to NbO₂, while it is 2.67 when Nb is oxidized to Nb₂O₅ (Ref 38). The P.B. ratio of Fe is 2.14 when Fe is oxidized to Fe₂O₃. The P.B. ratio of Zr is 1.56 when Zr is oxidized to ZrO₂. In this study, the main type of SPPs of the Zr-1Nb alloys containing Fe is [Zr-Nb-Fe] SPPs. As the content of Fe in the alloys increases, the Nb/Fe ratio of SPPs in the Zr-1Nb alloys containing Fe decreases. So it is signified that the stress produced at the interface between SPPs and oxide film is lower when [Zr-Nb-Fe] of a lower Nb/Fe ratio is oxidized than [Zr-Nb-Fe] SPPs of a higher Nb/Fe ratio. Crescent-shaped cracks are often observed on the side of the SPPs opposite to the O/M interface (Ref 39, 40) due to the additional stress created by the oxidation of SPPs (Ref 41, 42). Defects diffuse, annihilate and condensate under the effect of stress to form pores and micro-cracks in the oxide layer. Consequently, the oxide layer becomes loose, and thus, the corrosion accelerates (Ref 35), (Ref 43-45). [Zr-Nb-Fe] SPPs with a lower Nb/Fe ratio may be the one factor for the improvement on corrosion resistance of the alloys. There are also research results showing that the corrosion weight gain increases with the increase of Nb/Fe (Ref 23), (Ref 46, 47), which is consistent with the results in this paper.

The excessive Fe would promote the formation of coarse precipitates like Zr₂Cu and Zr₃Ge. The large size of Zr₃Ge would weaken the consistency between Zr₃Ge and ZrO₂ matrix. It would produce defects during oxide growth, which would accelerate the progress of microstructural evolution and destroy the integrity of oxide film to weaken the protection of oxide film (Ref 24, 25). The coarse SPPs have negative effect on the corrosion resistance of the alloys in superheated steam at 400 °C/10.3 MPa.

5. Conclusions

The corrosion resistance of the Zr-1Nb alloys containing Fe is improved significantly by Fe addition (in a range of 0.1 ~ 0.35) in superheated steam at 400 °C/10.3 MPa. The Zr-1Nb-0.35Fe-0.05Cu-0.05Ge alloy shows the best corrosion resistance among the alloys in this study. While most SPPs in the Zr-1Nb alloys containing Fe are [Zr-Nb-Fe]-type, some of them are β-Nb-type. As the content of Fe increases, the main

SPPs change gradually from h-Zr(NbFe)₂ to a mixture of h-Zr(NbFe)₂ and f-Zr(NbFe)₂ SPPs.

The process of micro-pores developing into micro-cracks and the evolution from columnar grains to equiaxed grains in the oxide film could be delayed by the addition of Fe. [Zr-Nb-Fe]-type SPPs are oxidized into amorphous phases, which can delay the structure transformation of oxide film.

Acknowledgments

The authors would like to thank Mr. Yuliang Chu, Jianchao Peng, Xue Liang, and Dr. Pengfei Hu for their assistance in the microstructure analysis. This study is supported by National Natural Science Foundation of China (No.51871141).

References

1. J.Z. Liu, *Structure nuclear materials*, Chemical Industry Press, Beijing, 2007
2. W. J. Zhao, B.X. Zhou, Z. Miao, Q. Peng, Y. R. Jiang, H. M. Jiang, H. Pang, Development of Chinese Advanced Zirconium Alloys, *Atom. Energ. Sci. Technol.* 2005, z1 2-9.
3. L.Y. Chen, J.X. Li, Y. Zhang, L.C. Zhang, W.J. Lu, L.F. Zhang, L.Q. Wang and D. Zhang, Effects of Alloyed Si on the Autoclave Corrosion performance and Periodic Corrosion Kinetics in Zr-Sn-Nb-Fe-O Alloys, *Corro. Sci.*, 2015, **100**, p 651-662.
4. Y. Li, P.K. Liaw and Y. Zhang, Microstructures and Properties of the Low-Density Al15Zr40Ti28Nb12M(Cr, Mo, Si)5 High-Entropy Alloys, *Metals*, 2022, **12**, p 496.
5. J. Lin, X.H. Cao and J.A. Szpunar, The Influence of the Texture and Microstructure of a Zr2.5Nb Substrate Upon the Oxidation Kinetics, *Mater. Sci. Forum*, 2002, **408**, p 1013-1018.
6. J.L. Liu, G. He, A. Callow, K.X. Li, K.L. Moore, H. Nordin, M. Moody, S. Lozano-Perez and C.R.M. Grovenor, The Role of β-Zr in a Zr-2.5Nb Alloy During Aqueous Corrosion: A Multi-Technique Study, *Acta Mater.*, 2021, **215**, p 117042.
7. Z.K. Li and J. Zhou, *Zirconium Industry Conference Collected Papers in [C]*, Metallurgical Industry Press (in Chinese), Beijing, 2008
8. W.Q. Liu, X.Y. Zhu, X.J. Wang, Q. Li, M.Y. Yao and B.X. Zhou, Effect of Nb and Fe on Corrosion Resistance of Zirconium Alloys, *Atom. Energ. Sci. Technol.*, 2010, **12**, p 1477-1481.
9. A. Yilmazbayhan, E. Breval, A.T. Motta and R.J. Comstock, Transmission Electron Microscopy Examination of Oxide Layers Formed on Zr Alloys, *J. Nucl. Mater.*, 2006, **349**, p 265-281.
10. B. Wadman, Z. Lai, H. O. Andren, A. L. Nystroem, P. Ruding, and H. Pettersson, Microstructure of Oxide Layers Formed During Autoclave Testing of Zirconium Alloys. Zirconium in the Nuclear Industry: Tenth International Symposium, ASTM STP (1994)
11. Y.H. Jeong, H.G. Kim and T.H. Kim, Effect of β Phase, Precipitate and Nb-Concentration in Matrix on Corrosion and Oxide Characteristics of Zr-xNb Alloys, *J. Nucl. Mater.*, 2003, **317**, p 1-12.
12. B. Gabory, A.T. Motta and K. Wang, Transmission Electron Microscopy Characterization of Zircaloy-4 and ZIRLO™ Oxide Layers, *J. Nucl. Mater.*, 2015, **456**, p 272-280.
13. W.J. Gong, H.L. Zhang, Y. Qiao, H. Tian, X.D. Ni, Z.K. Li and X.T. Wang, Grain morphology and Crystal Structure of Pre-transition Oxides Formed on Zircaloy-4, *Corros. Sci.*, 2013, **74**, p 323-331.
14. G. Cao, L. Yang, G. Yuan, Hu. Junhua, G. Shao and L. Yan, Chemical Diversity of Iron Species and Structure Evolution During the Oxidation of C14 Laves Phase Zr(Fe,Nb)₂ in Subcritical Environment, *Corros. Sci.*, 2020, **162**, p 108218.
15. B.N. Mordiyuk, O.P. Karasevskaya, G.I. Prokopenko and N.I. Khripta, Ultrafine-grained Textured Surface Layer on Zr-1% Nb Alloy Produced by Ultrasonic Impact Peening for Enhanced Corrosion Resistance, *Surf. Coat. Technol.*, 2012, **210**, p 54-61.
16. B.N. Mordiyuk, O.P. Karasevskaya and G.I. Prokopenko, Structurally Induced Enhancement in Corrosion Resistance of Zr-2.5% Nb Alloy in Saline Solution by Applying Ultrasonic Impact Peening, *Mater. Sci. Eng.: A*, 2013, **559**, p 453-461.

17. N.I. Khripta, O.P. Karasevska and B.N. Mordiyuk, Surface Layers of Zr-18% Nb Alloy Modified by Ultrasonic Impact Treatment: Microstructure, Hardness and Corrosion, *J. Mater. Eng. Perform.*, 2017, **26**, p 5446–5455.
18. J. Zhang, H. Yang, T. Liming, F. Sun, M. Yao and B. Zhou, Corrosion Behavior and Oxide Microstructure of Zr-1Nb-xGe Alloys Corroded in 360 °C/18.6 MPa Deionized Water, *Corros. Sci.*, 2016, **102**, p 161–167.
19. S.L. Li, M.Y. Yao, X. Zhang, J.C. Peng, J.Q. Geng and B.X. Zhou, Effect of Cu Addition on Corrosion Resistance of M5 Alloy in Superheated Steam at 500 °C, *Acad. Conf. China. Nucl. Soc.*, 2009, **1**, p 197–203
20. O.T. Woo and M. Griffiths, The Role of Fe on the Solubility of Nb in α -Zr, *J. Nucl. Mater.*, 2009, **384**, p 77–80.
21. F. Garzarolli, H. Stehle and E. Steinberg, A Short Review of Pertinent Aspects in LWR Fuel, *Zirconium in the Nuclear Industry*. E.R. Bradley, G.P. Sabol Ed., Eleventh Symposium, ASTM STP 1295, 1996, p 12–32
22. R.S. Wang, K.W. Li, Y.W. Zhang, J.Q. Geng, X.D. Chen and E.W. Liu, Effect of Fe on the Precipitate Characteristics and Out-of-Pile Corrosion Behavior of Zr-1Nb-xFe Alloys, *Mater. Sci. Forum*, 2013, **744**, p 1–7.
23. Y. Lin, Conventional corrosion behavior of Zr-xNb-yM(M=Fe, Cr) alloy and high temperature steam oxidation behavior under simulated LOCA, Shanghai University, Shanghai, 2020. **(in Chinese)**
24. M. Schaffer, B. Schaffer and Q. Ramasse, Sample Preparation for Atomic-Resolution STEM at Low Voltages by FIB, *Ultramicroscopy*, 2012, **114**, p 62–71.
25. M.K. Miller, K.F. Russell, K. Thompson, R.L. Alvis and J. David, Larson Review of Atom Probe FIB-Based Specimen Preparation Methods, *Microsc. Microanal.*, 2007, **13**(6), p 428–436.
26. J.L. Zhang, X.F. Xie and M.Y. Yao, Effect of Ge Addition on Corrosion Performance of Zr-4 Alloy in Lithiated Solution, *Chin. J. Nonferrous Met.*, 2013, **23**(6), p 1542–1548. **(in Chinese)**
27. J.L. Zhang, L.M. Tu, X.F. Xie, M.Y. Yao and B.X. Zhou, Corrosion Resistance of Zr-1Nb-xGe Alloys in Superheated Steam at 400°C, *J.Cn. Soc. For. Corros. Pro.*, 2014, **34**, p 171–177. **(in Chinese)**
28. N. Ni, S. Lozano-Perez, M.L. Jenkins, C. English, G.D.W. Smith, J.M. Sykes and C.R.M. Grovenor, Porosity in Oxides on Zirconium Fuel Cladding Alloys, and its Importance in Controlling Oxidation Rates, *Scr. Mater.*, 2010, **62**, p 564–567.
29. Jianzhang Liu, Nuclear Structural Material [M]. Chemical Industry Press, 2007, **(in Chinese)**
30. Y.H. Jeong, H.G. Kim, D.J. Kim, B.K. Choi and J.H. Kim, Influence of Nb Concentration in the α -Matrix on the Corrosion Behavior of Zr-xNb Binary Alloys, *J. Nucl. Mater.*, 2003, **323**, p 72–80.
31. H. Anada, K. Takeda, Microstructure of Oxides on Zircaloy-4, 1.0Nb Zircaloy-4, and Zircaloy-2 Formed in 10.3-MPa Steam at 673 K, Zirconium in the Nuclear Industry: 11th International Symposium, ASTM STP 1295, (1996)35–54
32. W.J. Gong, H.L. Zhang, C.F. Wu, H. Tian and X.T. Wang, The Role of Alloying Elements in the Initiation of Nanoscale porosity in Oxide Films Formed on Zirconium Alloys, *Corros. Sci.*, 2013, **77**, p 391–396.
33. L. X, *Study on the effect of Sn*, Thesis, Shanghai University, Shanghai, Fe on the corrosion resistance of zirconium alloy, 2014. **(in Chinese)**
34. G. Choudhuri, M.K. Jagannath, V. Kumar, D. Kain, S. Srivastava, B.K. Basu, N. Shah and G.K. Saibaba, Dey, Influence of Fe Content on Corrosion and Hydrogen Pick up Behavior of Zr–2.5Nb Pressure Tube Material, *J. Nucl. Mater.*, 2013, **441**, p 178–189.
35. B.X. Zhou, Q. Li, M.Y. Yao, W.Q. Liu and Y.L. Chu, Effect of Water Chemistry and Composition on Microstructural Evolution of Oxide on Zr Alloys, Zirconium in the Nuclear Industry: 15th International Symposium, *ASTM STP*, 2009, **1505**, p 360–380.
36. H.G. Kim, J.Y. Park and Y.H. Jeong, Ex-reactor Corrosion and Oxide Characteristics of Zr–Nb–Fe Alloys with the Nb/Fe Ratio, *J.Nucl. Mater.*, 2005, **345**, p 1–10.
37. X.X. Cao, *Second phase alloys in zirconium alloys* Corrosion Behavior Study, Shanghai University, Shanghai, Thesis, 2010. **(in Chinese)**
38. C. Proff, S. Abolhassania and C. Lemaignan, Oxidation Behaviour of Zirconium Alloys and Their Precipitates – A Mechanistic Study, *J. Nucl. Mater.*, 2013, **432**, p 222–238.
39. N. Ni, S. Lozano-Perez, J.M. Sykes, G.D.W. Smith and C.R.M. Grovenor, Focussed ion Beam Sectioning for the 3D Characterisation of Cracking in Oxide Scales Formed on Commercial ZIRLO™ Alloys During Corrosion in High Temperature Pressurisedwater, *Corros. Sci.*, 2011, **53**, p 4073–4083.
40. C. Proff, S. Abolhassania and C. Lemaignan, Oxidation Behaviour of Binary Zirconium Alloys Containing Intermetallic Precipitates, *J. Nucl. Mater.*, 2011, **416**, p 125–134.
41. M. Preuss, P. Frankel, S. Lozano-Perez, D. Hudson, E. Polatidis, N. Ni, J. Wei, C.English, S. Storer, K.B. Chong, M. Fitzpatrick, P. Wang, J. Smith, C. Grovenor, G. Smith, J. Sykes, B. Cottis, S. Lyon, L. Hallstadius, R.J. Comstock, A. Ambard, M. Blat-Yrieix, Studies Regarding Corrosion Mechanisms in Zirconium Alloys, 16th International Symposium on Zirconium in the Nuclear Industry, 1529, ASTM STP, 2011, pp. 649–681
42. B. Griggs, H.P. Maffei and D.W. Shannon, Multiple Rate Transitions in the Aqueous Corrosion of Zircaloy, *Electro. Chem. Soc.*, 1962, **109**, p 665–668.
43. B.X. Zhou, Q. Li, W.Q. Liu, M.Y. Yao and Y.L. Chu, The Effects of Water Chemistry and Composition on the Microstructure Evolution of Oxide Films on Zirconium Alloys during Autoclave Tests, *Rare Metal. Mat. Eng.*, 2006, **35**, p 1009–1016. **(in Chinese)**
44. B.X. Zhou, Q. Li, M.Y. Yao, W.Q. Liu and Y.L. Chu, Study on Microstructure of Zr-4 Alloy Oxide Film, *J.Cn. Corrosion. Protection.*, 2009, **30**, p 589–594. **(in Chinese)**
45. B.X. Zhou, Q. Li, M.Y. Yao, W.Q. Liu and Y.L. Chu, Microstructure Evolution of Oxide Films of Zirconium-4 Alloys Corroded in Autoclave, *Nucl. Power Eng.*, 2005, **26**, p 364–371. **(in Chinese)**
46. Z.B. Yang, W.J. Zhao, Z.Q. Cheng, J.Q.H. Zhang and H. Zhuo, Corrosion Resistance of Zr-xNb-Sn-Fe Alloy in Superheated Steam, *Acta. Metall. Sin.*, 2017, **53**, p 47–56. **(in Chinese)**
47. L.Y. Chen, P. Shen, L. Zhang, L. Sheng, L. Chai, Z. Yang and L.C. Zhang, Corrosion Behavior of Non-equilibrium Zr-Sn-Nb-Fe-Cu-O Alloys in High-temperature 0.01 M LiOH Aqueous Solution and Degradation of the Surface Oxide Films, *Corros. Sci.*, 2018, **136**, p 221–230.

Publisher's Note Springer Nature remains neutral with regard to jurisdictional claims in published maps and institutional affiliations.